

Orbital-selective effect of spin reorientation on the Dirac fermions in a three-dimensional kagome ferromagnet Fe_3Ge

Rui Lou^{1,2,3,*,†}, Liqin Zhou^{4,6,*}, Wenhua Song^{5,*}, Alexander Fedorov^{1,2,3,*}, Zhijun Tu^{5,*}, Bei Jiang^{4,6}, Qi Wang^{5,7,8}, Man Li⁹, Zhonghao Liu^{10,11}, Xuezhi Chen^{6,12}, Oliver Rader², Bernd Büchner^{1,13}, Yujie Sun¹⁴, Hongming Weng^{4,6,15,‡}, Hechang Lei^{5,§} & Shancai Wang^{5,¶}

¹*Leibniz Institute for Solid State and Materials Research, IFW Dresden, 01069 Dresden, Germany*

²*Helmholtz-Zentrum Berlin für Materialien und Energie, Albert-Einstein-Straße 15, 12489 Berlin, Germany*

³*Joint Laboratory “Functional Quantum Materials” at BESSY II, 12489 Berlin, Germany*

⁴*Beijing National Laboratory for Condensed Matter Physics and Institute of Physics, Chinese Academy of Sciences, Beijing 100190, China*

⁵*Department of Physics, Key Laboratory of Quantum State Construction and Manipulation (Ministry of Education), and Beijing Key Laboratory of Opto-electronic Functional Materials & Micro-nano Devices, Renmin University of China, Beijing 100872, China*

⁶*University of Chinese Academy of Sciences, Beijing 100049, China*

⁷*School of Physical Science and Technology, ShanghaiTech University, Shanghai 201210, China*

⁸*ShanghaiTech Laboratory for Topological Physics, ShanghaiTech University, Shanghai 201210,*

*These authors contributed equally to this work.

†lourui09@gmail.com

‡hmweng@iphy.ac.cn

§hlel@ruc.edu.cn

¶scw@ruc.edu.cn

China

⁹*School of Information Network Security, People's Public Security University of China, Beijing 100038, China*

¹⁰*National Key Laboratory of Materials for Integrated Circuits, Shanghai Institute of Microsystem and Information Technology, Chinese Academy of Sciences, Shanghai 200050, China*

¹¹*Center of Materials Science and Optoelectronics Engineering, University of Chinese Academy of Sciences, Beijing 100049, China*

¹²*Shanghai Institute of Applied Physics, Chinese Academy of Sciences, Shanghai 201800, China*

¹³*Institute for Solid State and Materials Physics, TU Dresden, 01062 Dresden, Germany*

¹⁴*Department of Physics, Southern University of Science and Technology, Shenzhen 518055, China*

¹⁵*Songshan Lake Materials Laboratory, Dongguan, Guangdong 523808, China*

Kagome magnets provide a fascinating platform for the realization of correlated topological quantum phases under various magnetic ground states. However, the intricate effect of the magnetic spin configurations on the characteristic electronic structure directly from the kagome lattice layer remains still elusive. Here, utilizing angle-resolved photoemission spectroscopy and density functional theory calculations, we report the spectroscopic evidence for the spin-reorientation effect of a kagome ferromagnet Fe_3Ge , which is composed only of the kagome planes. There are two kinds of kagome-derived Dirac fermions due to the structural three-dimensionality – one is less dispersive ($k_z \sim 0$) and the other disperses linearly ($k_z \sim \pi$). As the Fe moments cant from the c axis into the ab plane upon cooling, the Dirac fermion in $k_z \sim 0$ plane with a mixture of the $\text{Fe-}3d_{xy}$ and $\text{Fe-}3d_{x^2-y^2}$ components evolves from gapped into nearly gapless, while the Dirac cone in $k_z \sim \pi$ plane mainly of the $\text{Fe-}3d_{x^2-y^2}$ orbital character remains intact, suggesting that the effect of spin reorientation on the Dirac fermions has an orbital selectivity. Our unambiguous observations provide a feasible route to design and manipulate the mass of Dirac fermions for realizing the novel quantum phases. We also perform comparative studies between the non-charge-ordered Fe_3Ge and its sibling compound FeGe , a newly established charge-density-wave kagome magnet, the results suggest that the orbital-selective van Hove singularities near the Fermi level play an indispensable part in driving the charge order on a magnetic kagome lattice.

The entanglement of multiple degrees of freedom including spin, charge, and lattice is widely believed to be responsible for the rich phase diagrams in correlated systems, where the various ordered phases being closely adjacent to each other allow the continuous tunability of the ground states^{1,2}. The similar case with an intertwining between nontrivial band topology, magnetism, and symmetry-breaking states has been recently discovered in the *3d* transition-metal-based kagome lattices. The frustrated lattice geometry of a kagome lattice can give rise to the unique electronic structure embracing the flat band (FB) over the entire Brillouin zone (BZ), the Dirac point (DP) at the BZ corner, and the van Hove singularities (vHSs) at the BZ boundary. A further combination of the frustrated lattice geometry and the intrinsic magnetism has been reported to engender a variety of novel quantum phenomena, such as the massive Dirac fermions³ and skyrmion bubble states⁴ in ferromagnetic (FM) Fe₃Sn₂; the spin-polarized FB in antiferromagnetic (AFM) FeSn^{5,6}; the magnetic Weyl fermions and large anomalous Hall effect in non-collinear AFM Mn₃Sn^{7,8} and Mn₃Ge^{9,10}; the topological Chern magnetism in FM TbMn₆Sn₆¹¹; and the FM Weyl semimetal state in Co₃Sn₂S₂¹²⁻¹⁴. In addition to these magnetic compounds, the recent discovery of kagome superconductors AV₃Sb₅ (*A* = K, Rb, Cs) has also expanded the family of non-magnetic kagome metals¹⁵⁻²⁵. Significant interests have been focused on the time-reversal symmetry-breaking charge density wave (CDW) therein²⁶⁻³², which could be triggered by the interactions between multiple vHSs close to the Fermi level (E_F)³³⁻³⁷. Very recently, a three-dimensional (3D) CDW order with the same $2 \times 2 \times 2$ superstructure as AV₃Sb₅ was observed deep inside the AFM phase of a correlated kagome metal FeGe³⁸⁻⁴⁰. The electronic instabilities might still play a role in the formation of CDW therein, as the vHSs are found to be shifted to the vicinity of E_F by the AFM

order⁴¹. This magnetism-induced band modification provides a precious opportunity to explore the magnetic impact on the characteristic electronic structure of the kagome lattice. However, the presence of two types of terminations in FeGe (Ge and kagome terminations³⁹) makes it less conducive to designing and manipulating the band structure that is intrinsic to the kagome lattice layer by the magnetic exchange interactions.

Here, we combine angle-resolved photoemission spectroscopy (ARPES) and density functional theory (DFT) calculations to study the effect of spin reorientation on the electronic structure of a kagome ferromagnet Fe₃Ge. Compared to the structure of FeGe, where the neighbouring Fe₃Ge kagome layers are well separated by the Ge honeycomb layer^{42,43}, the Fe₃Ge compound consists only of the directly stacked Fe₃Ge kagome layers, as shown in Fig. 1a. We find that the structural three-dimensionality of Fe₃Ge is reflected in its electronic structure featuring 3D characters, particularly in the two kagome-derived Dirac fermions with different k_z values exhibiting distinct dispersions. Moreover, we reveal that these two Dirac fermions show different responses as the Fe moments cant from the c axis into the ab plane⁴⁴ – the first (DP1) formed by the less-dispersive bands ($k_z \sim 0$) evolves from gapped into nearly gapless; while the second (DP2) with the linear band dispersions ($k_z \sim \pi$) is much less affected. According to the orbital-resolved DFT calculations, the DP1 has a mixture of the Fe- $3d_{xy}$ and Fe- $3d_{x^2-y^2}$ orbitals and the DP2 is mainly composed of the Fe- $3d_{x^2-y^2}$ orbital. These results taken together indicate the orbital-selective effect of spin reorientation on the Dirac fermions. We further find that there is no signature of CDW order formation in Fe₃Ge. The electron correlations and the nesting of vHSs have been quantitatively examined. The comparative studies of Fe₃Ge and FeGe suggest an essential role of the

orbital-selective vHSs near E_F in triggering the CDW instabilities. Our work not only sheds light on the origin of the CDW order in magnetic kagome metals, but also establishes the first kagome system in which the mass of Dirac fermion can be controlled by the intrinsic magnetism. The high possibility of switching the Dirac electrons in Fe_3Ge by external magnetic fields paves the way to new functionalities.

Fe_3Ge is isostructural to Mn_3Sn ^{7,8} and Mn_3Ge ^{9,10}, crystalizing in a hexagonal structure with the $P6_3/mmc$ (No. 194) space group and belonging to the kagome lattice binary T_mX_n series ($T = \text{Mn, Fe, Co}$; $X = \text{Sn, Ge}$; $m:n = 3:1, 3:2, 1:1$)⁵. Like the Mn_3Ge bulk crystals⁴⁵, we found that it is almost unfeasible to obtain atomically flat surfaces for the surface-sensitive ARPES experiments by cleaving the single crystals of Fe_3Ge . We thus polished the (001) surfaces of Fe_3Ge crystals and then sputtered and annealed the polished surfaces in the vacuum⁴⁶. The sputtering and annealing procedures were repeated several times until we observed clear low-energy electron diffraction (LEED) patterns, as shown in Fig. 1b and Supplementary Fig. S1. The treated sample surfaces have been further characterized by X-ray photoelectron spectroscopy measurements (Supplementary Fig. S2), where the doublet structures of Ge- $3d_{3/2}$ and Ge- $3d_{5/2}$ core levels are identified, pointing to the bulk-surface splitting. A uniaxial FM ordering with moments oriented along the z axis was found to appear below $T_c \approx 650$ K in hexagonal Fe_3Ge ⁴⁷, the magnetization directions here and hereafter are described in the Cartesian coordinates (the setup of the x , y , and z axes relative to the a , b , and c axes is sketched in the inset of Fig. 1a). As depicted in Fig. 1c, it was reported that the Fe moments start to cant away from the z axis towards the xy plane at a lower temperature of $T_{SR} \approx 380$ K and finally a planar FM ground state is formed⁴⁴ (below T_{planar}

~ 170 K, which is determined by our ARPES results presented below).

Figure 1d shows the bulk and (001)-projected surface BZs of Fe_3Ge . Along the high-symmetry directions marked out in Fig. 1d (red solid lines), we plot the overall bulk band structure from DFT calculations in the FM state in Fig. 1e-g, where the preferred spin direction is along the x , y , and z axis, respectively (the calculated magnetic moment of $\sim 2.2 \mu_{\text{B}}/\text{Fe}$ is close to the previous experimental value of $\sim 2.0 \mu_{\text{B}}/\text{Fe}$ ⁴⁴). Below E_{F} , a FB over the whole BZ and two sets of DPs and vHSs (denoted as DP1,2 and vHS1,2) are identified. We find that these kagome bands are shifted much further below E_{F} upon entering the paramagnetic phase (Supplementary Fig. S3), similar to the case of FeGe ⁴¹. The structural three-dimensionality of the kagome lattice gives rise to quite different electronic structures in the $k_z = 0$ and π planes, in particular the gapped Dirac fermions DP1 and DP2, which are formed by the less-dispersive bands and linear band dispersions, respectively. Interestingly, as the reorientation of spin from the xy plane (Fig. 1e,f) towards the z axis (Fig. 1g), one notices that these two Dirac fermions respond differently, with the Dirac gap at DP1 being remarkably enhanced (from ~ 0.5 to ~ 60 meV) and the Dirac gap at DP2 being less affected (from ~ 120 to ~ 100 meV).

In order to characterize the typical kagome electronic structure in the planar FM state, we carried out the polarization- and photon-energy-dependent ARPES measurements on the (001) surfaces of Fe_3Ge . The key signatures of the kagome lattice are summarized in Fig. 2. According to the ARPES intensity map in the $h\nu$ - k_{\parallel} plane (Supplementary Fig. S4a), we determine that the photon energies of 125 and 146 eV are respectively close to the k_z values of 0 and π . In Fig. 2a, we

present the Fermi surface (FS) intensity plot in the $k_z \sim 0$ plane. There exist two hole-like pockets centered at Γ point, consistent with the DFT calculations (Fig. 2c and Supplementary Fig. S5). The outer FS is vanishingly weak along the Γ - K direction of the first BZ while is more visible in the second BZ due to matrix element effects. As shown in Fig. 2b and Supplementary Fig. S4b-e, the FS mapping recorded near the $k_z \sim \pi$ plane displays a richer topology than that of the $k_z \sim 0$ plane. The most prominent feature therein is a circular electron-like pocket around H point, which arises out of the kagome-lattice-derived Dirac bands of the DP2. The Dirac cone structure can be directly visualized in a series of constant energy maps in Fig. 2b. Along with the energy going below E_F , the circular FS contour (guided by the red circle) first shrinks into a single point at $E \approx -0.10$ eV and then expands out again.

To further study the underlying dispersions of the DP2, we measured the near- E_F ARPES spectra along the H - L - H direction. As shown in Fig. 2d,e, the linear bands cross each other at about -0.10 eV to form the DP2 at H point, agreeing with the evolution of Dirac fermiology in Fig. 2b. We further observe that the lower branch from DP2 disperses down to form the vHS2 at about -0.35 eV at L point, as expected from the kagome tight-binding model⁴⁸⁻⁵⁰. Besides this set of DP and vHS, we also identify the DP1 (at about -0.13 eV, K point) and vHS1 (at about -0.11 eV, M point) in the $k_z \sim 0$ plane (Fig. 2f,g). Because of the small difference in the binding energies of DP1 and vHS1 as well as the DP1 consisting of less-dispersive bands as suggested by the DFT calculations, the dispersion that connects the DP1 and vHS1 is nearly flat and almost indistinguishable from the lower branch of DP1 along the K - M direction, as shown in Fig. 2f and 3a. But it should be noted that this flatness is not related to the destructive phase interference of

Bloch wave functions in a kagome lattice, which gives rise to the FBs spanning the entire BZ⁵. The saddle-point topology of the vHS1 can be clearly visualized by tracing the dispersions across M point. In Fig. 2h, we therefore display a series of cuts parallel to the K - M - K direction (indicated by the black dashed arrows in Fig. 2a,h), the band tops of the hole-like band (guided by the red solid curve) show a minimum energy at about -0.11 eV at M point, tracing out an electron-like band (red dashed curve) in the orthogonal direction (Γ - M direction). In addition to the DP1 and vHS1, we further observe a broad band (at around -0.5 eV) that is nearly dispersionless over a wide range of momentum, as indicated by the blue shades in Fig. 2f,g. The energy location of this feature matches that of the kagome FB in DFT calculations (Fig. 1e,f), implying that it is of the phase-destructive-FB origin⁵. The FB nature can be better visualized by tracing the peak positions in the corresponding energy distribution curves (EDCs) (Supplementary Fig. S6a,b). One can identify the FB feature also under different photon polarization (Supplementary Fig. S6c,d) and photon energy (Supplementary Fig. S6e,f), further showing that the FB is intrinsic to the kagome lattice.

Having fully characterized the typical band structure of the kagome lattice, we now examine the intricate effect of spin reorientation on the electronic structures via the temperature-dependent ARPES measurements. Figure 3a summarizes the experimental band dispersions along the Γ - M - K - Γ lines deep inside the planar FM state ($T = 16$ K, $h\nu = 125$ eV), the results match well with the DFT calculations (upper panel of Fig. 3b), in particular the near- E_F bands that are marked out. The calculations suggest that the reorientation of spin mainly modifies the Dirac band gap at the DP1 (Fig. 1e-g and 3b). Since the labeled vHS1 and α , β , γ bands, which connect to the upper

or lower branch of the DP1, might also be modified accordingly, we thus study the temperature evolutions of these features together with the DP1. As indicated by the cyan markers in Fig. 3a, we plot the corresponding EDCs (ellipse, triangle, and star markers) and momentum distribution curves (MDCs) (capsule-like marker) at various temperatures in Fig. 3c-f, where the temperatures are illustrated using the same colours as the labels of Fig. 3g.

As shown in Fig. 3c, when we increase the temperature from 16 to 170 K, the EDC peak position of the DP1 remains at a constant energy (about -0.13 eV), compatible with the nearly gapless nature (~ 0.5 meV) of the DP1 in the planar FM state expected from the DFT calculations (upper panel of Fig. 3b). Upon further warming up the sample to 210 K, one obtains that the single EDC peak of the DP1 is clearly split into a double-hump structure, pointing to a gap opening of ~ 50 meV (see the reproducibility of the temperature evolution and the quantitative extraction of the gap size in Supplementary Fig. S7). This remarkable change of the band gap at the DP1 indicates that the Fe moments start to cant away from the xy plane towards the z axis at around 170 K. The spectroscopic response to the spin-reorientation effect can also be revealed at the bottom of the γ band, whose momentum location is denoted as K' point (Fig. 3a). By tracing the peak positions of the EDCs through K' point (Fig. 3d), one observes that the γ band bottom is slightly pushed down ~ 15 meV (highlighted by the black arrow) once the temperature is increased from 170 to 210 K. This behaviour is consistent with our DFT calculations, where the downward movement of the lower branch of the DP1 upon the gap enlargement pushes the γ band bottom to a slightly higher binding energy (Fig. 3b). Based on these spectroscopic evidences, we sketch the magnetic phase diagram of Fe_3Ge in Fig. 3g.

Figure 3e,f shows the temperature dependence of the vHS1 and α , β bands. In contrast to the DP1 and γ band, the bottoms of the α (i.e., the vHS1, at about -0.11 eV) and β (at about -0.20 eV) bands at M point are less temperature sensitive as evidenced by the EDCs in Fig. 3e. We further look into the Fermi crossings of α and β bands via the MDCs along the Γ - M direction taken at E_F . To better visualize their temperature behaviour, we artificially align one of the α , β bands branches at various temperatures to a certain momentum position, respectively, as indicated by the two red solid lines in Fig. 3f. The MDC peaks from the other branches are both observed to gradually shift towards M point as the temperature is lowered (guided by the two red dashed lines in Fig. 3f). These facts taken together suggest that the Fermi velocities (the effective masses) of α and β bands are increased (reduced) upon cooling, whose implications will be discussed later.

Next, we proceed to the temperature-dependent study of the electronic structures in the $k_z \sim \pi$ plane. Figure 3h displays the band dispersions along the A - H - L lines ($T = 16$ K, $h\nu = 146$ eV), where the DP2 and a hole-like band top (δ) are identified at H and L points, respectively, consistent with that in Fig. 2d,e and the DFT calculations (Fig. 1e,f). As seen in the calculations (Fig. 1e-g), the spin-reorientation effect only induces the small degeneracy lifting of some bands in the $k_z = \pi$ plane (like the dispersions related to the DP2), which could be beyond the capability of our measurements. Accordingly, from the EDCs and MDCs at various temperatures, we do not see visible change in the binding energies for the DP2 (at about -0.10 eV) and δ band (at about -0.06 eV) (Fig. 3i,j), as well as the Fermi wave vector (k_F) for the upper branch of the DP2 (i.e., the η band, Fig. 3k). One notices that the Dirac gap at the DP2 predicted by the calculations (Fig. 1e-g) is not identified in the experiments (Fig. 3h,i). The k_z broadening effect is found to be significant

in the vacuum ultraviolet ARPES, where the spectra reflect the electronic states integrated over a certain k_z region of the bulk BZ^{51,52}. We find that here the ARPES intensity in the $k_z \sim \pi$ plane could suffer from a larger k_z broadening effect than the $k_z \sim 0$ plane, because the spectra taken with 135-eV photons, which correspond to the k_z value of $\sim \pi/2$, still show many similarities with that from the $k_z \sim \pi$ plane, as seen in Fig. 2d,e and Supplementary Fig. S4. In this context, the Dirac cone structure of the DP2 observed in the $k_z \sim \pi$ plane actually also contains the projections from the nearby k_z planes, which could host the Dirac cones with slightly different dispersions (see the additional FS pockets at H point in Supplementary Fig. S4b,c). As a result, the Dirac gap at the DP2 could be smeared out by the k_z projections.

To reveal the origin of the distinct responses of these two Dirac fermions (DP1 and DP2) to the spin-reorientation effect, we carried out the orbital-projected DFT calculations in the planar FM state, as presented in Fig. 4. By comparing the orbitally-resolved Fe-3d (Fig. 4a,b) and Ge-4p (Fig. 4c,d) band structures, one finds that the energy bands around E_F are dominated by the Fe-3d orbitals (as also seen in the density-of-states (DOS) calculations in Supplementary Fig. S8), similar to the case of FeGe^{41,53} and FeSn^{5,54,55}. Furthermore, we identify that the DP1 and vHS1 are mainly contributed by a combination of the Fe-3d_{xy} and Fe-3d_{x²-y²} orbitals, while the DP2 and vHS2 are primarily associated with the Fe-3d_{x²-y²} orbital. The Dirac fermions composed of different orbital characters have also been reported in other 3d transition-metal kagome magnets^{5,6,41,53,56-58}, where, however, the Dirac fermions of the in-plane orbitals are usually observed to have a twofold degeneracy of the 3d_{xy} and 3d_{x²-y²} orbitals (as seen in, for example, FeGe⁵³ and FeSn^{54,55}). Therefore, here the orbital differentiation between the DP1 and DP2 points

to a picture of orbital-selective response of the Dirac fermions to the spin-reorientation effect. On the other hand, the behaviour of the Dirac gap at DP1 resembles that of the Kane-Mele type spin-orbit coupling (SOC) gap⁵⁹, which is negligible under in-plane magnetic order while is strongly enhanced under out-of-plane magnetic order. This is reminiscent of the opening of a Chern gap for the spin-polarized Dirac fermions in kagome ferromagnet TbMn_6Sn_6 ¹¹. Therein, the combination of the out-of-plane magnetization and the Kane-Mele type SOC is suggested to be responsible for the large Chern gap. Thus, one can deduce that here the SOC effect of the $3d_{xy}$ electrons dominates the gap at the DP1 and should follow the Kane-Mele scenario, exhibiting a strong anisotropy. While for the SOC effect of the $3d_{x^2-y^2}$ electrons, we suggest that it should be negligible and contributes little to the predicted gap at the DP2, which is nearly independent of the magnetization direction (see detailed discussion in Supplementary Note 1). One possible source of this Dirac gap (DP2) is the spin chirality, which produces a gauge flux and has been proposed to be able to open a Dirac gap independent of the spin orientation^{60,61}. Future spin-resolved ARPES measurements are desired to reveal whether the dispersions of the DP2 have the chiral spin textures.

The emergent CDW state in kagome metals has drawn considerable attention^{62,63}. Differently from the weakly electron-correlated AV_3Sb_5 , where the CDW could be intimately related to the nesting of vHSs^{26,28,32,33}, in the moderately correlated FeGe, it has been proposed that not only the vHSs near E_F but also the electron correlation effects should be considered in understanding the origin of the CDW instabilities^{41,53,64}. We now examine these aspects as well as whether the CDW develops in Fe_3Ge and compare our results with those reported in FeGe.

We first study the strength of electron correlations in Fe_3Ge . We quantitatively compare the band features between experiments (at base temperature) and DFT calculations (planar FM state). The details are summarized in Supplementary Table S1. An overall renormalization factor of 2–3 is obtained, which is comparable with that in previous ARPES study of FeGe ⁴¹, showing that Fe_3Ge is also a moderately correlated compound. Then we examine the role of vHSs. The AFM exchange splitting in FeGe brings the vHSs to the vicinity of E_F and the CDW gap opening of ~ 20 meV is observed on the vHS bands⁴¹. The vHSs in both FeGe and AV_3Sb_5 are found to have orbital-dependent contributions to the CDW formation, where the $3d_{xz}/3d_{yz}$ orbitals are proposed to be dominant^{41,65}. In the case of Fe_3Ge , although we also see that the emergence of ferromagnetism brings the two sets of kagome bands closer to E_F (Supplementary Fig. S3), the vHS1 near E_F arises mainly from the in-plane orbital characters (Fig. 4a,b), it thus would not induce the electronic instabilities in Fe_3Ge . This point can also be illustrated by the zero-frequency joint DOS calculated from the autocorrelation of the experimental FS in the $k_z \sim 0$ plane (see details in Supplementary Note 2). The resulting joint DOS exhibits no peaks at M points (Supplementary Fig. S9a), indicating the absence of nesting between the vHS1. On the other hand, one sees that a vHS connecting to the upper branch of the DP2 has a non-negligible $3d_{xz}$ component (denoted as vHS3, Fig. 4a) and it is located closer to E_F than the vHS1 in experiments ($\sim 60 \pm 20$ meV above E_F depending on k_z , a parabolic fit to the occupied band η is used to estimate the location of vHS3, Supplementary Fig. S10d), seeming to have the potential to induce electronic instabilities. The autocorrelation map in the $k_z \sim \pi$ plane indeed shows peaks at L points (Supplementary Fig. S9b, the anisotropic amplitudes between the nominally equivalent L points might arise from ARPES

matrix elements), implying the existence of nesting between the vHS3 around $k_z \sim \pi$. However, in contrast to the quasi-two-dimensional (quasi-2D) electronic structures of FeGe^{38,41} and AV₃Sb₅⁶⁵, the highly 3D feature of Fe₃Ge could give rise to vHS3 being near E_F only in a small range of k_z . As a result, this nesting is most likely not sufficient to cause the charge fluctuations on the entire 3D FS. Thus, the vHS3 could not induce the electronic instabilities either.

Consistently, by plotting the temperature-dependent EDCs and symmetrized EDCs taken at k_F 's of the vHS1 and vHS3 bands (i.e., the α and η bands, respectively), no signature of CDW gap opening is observed around E_F , as shown in Supplementary Fig. S10b,c,e,f. The aforementioned enhancement of Fermi velocities for the α and β bands upon cooling also implies that there is no CDW gap at E_F , because their evolutions are incompatible with that of the Bogoliubov quasiparticles with back-bending dispersions around k_F . The absence of charge ordering is further evidenced by the electrical resistivity measurements in Supplementary Fig. S11, where Fe₃Ge shows a metallic behaviour without anomalies. These comparative studies of Fe₃Ge and FeGe have the following implications: given that the moderate electron correlations are present in both compounds while the vHS nesting is much stronger in FeGe^{38,41}, the electronic instabilities induced by the vHSs near E_F most likely play an indispensable part in the CDW; and accordingly, the quasi-2D structural characteristics, which prepares the seedbed for the nesting of vHSs, may be a prerequisite for the formation of CDW. Besides, we also deduce that, in the charge-ordered kagome magnets, there most likely exists the cooperative interplay between the electron correlations, electronic instabilities, and probably also electron-phonon coupling (a kink structure was observed on the vHS band in FeGe⁴¹ while not seen here in Fe₃Ge), which could be important not only in driving the CDW

but also in determining the unconventional behaviours of the CDW^{66,67}.

In summary, we have unambiguously revealed the orbital-selective effect of spin reorientation on the Dirac fermions in kagome ferromagnet Fe₃Ge. As the reorientation of spin from the *c* axis towards the *ab* plane, the less-dispersive Dirac fermion with the degenerate $3d_{xy}/3d_{x^2-y^2}$ orbital characters evolves from gapped into nearly gapless, while the linearly dispersing Dirac cone of the $3d_{x^2-y^2}$ orbital remains unchanged. The comparative studies between Fe₃Ge and FeGe further suggest the presence of orbital-selective vHSs near E_F as the vital ingredient for triggering the CDW transition in a magnetic kagome lattice.

The magnetic modification of the gapped Dirac fermion observed here is similar to the momentum-dependent Zeeman energy shift of the massive Dirac band in kagome magnet YMn₆Sn₆ driven by a magnetic field⁶⁸. Therein, the field-induced changes of the Dirac band point to a momentum-dependent Landé *g* factor. In the case of Fe₃Ge, due to the band dispersions of the Dirac fermion can already be manipulated by the spontaneous magnetization, an effective *g* factor with even more exotic behaviours, like the stronger momentum dependence, might be expected. In this context, an external magnetic field may further lead to unusual Zeeman energy shifts and band modifications in Fe₃Ge, enabling the fine tunability of the kagome electronic structure towards realizing more unconventional ground states.

Methods

Sample synthesis

Single crystals of Fe_3Ge were grown by chemical vapor transport method. Iron powder and germane powder were mixed in a ratio of 7:3, then were putted into evacuated fused quartz ampoule with I_2 as a transport agent. The transport reaction was carried out in a two-zone furnace with a temperature gradient of 1075 to 1175 K for two weeks. After reaction, the single crystals of Fe_3Ge can be obtained.

ARPES measurements

ARPES measurements were performed using the 1^2 -ARPES end station of UE-112-PGM2 beamline at Helmholtz Zentrum Berlin BESSY-II light source. The energy and angular resolutions were set to better than 5 meV and 0.1° , respectively. During the experiments, the sample temperature was kept at 16 K if not specified otherwise, and the vacuum conditions were maintained better than 6×10^{-11} Torr. In order to obtain atomically flat surfaces for the ARPES measurements, we polished the (001) surfaces of Fe_3Ge single crystals, and then repeatedly sputtered and annealed the samples using an argon ion source and the electron beam, respectively, until sharp LEED patterns appeared.

Band structure calculations

The electronic structure calculations were performed by the Vienna ab initio Simulation package with the projector augmented-wave formalism based on the DFT^{69,70}. The generalized gradient approximation with the Perdew-Burke-Ernzerhof type was adopted as the exchange-correlation functional⁷¹. The cutoff energy for the plane-wave basis was set to be 500 eV and the local mag-

netic moment on Fe atoms was along the x , y , and z axis for the FM state, respectively. An $10 \times 10 \times 12$ Γ -centered mesh was implemented for the BZ integral sampling. To get the tight-binding model Hamiltonian, we used the wannier90 package to obtain the maximally localized Wannier functions with Fe p and d orbitals⁷². The FSs of Fe₃Ge were calculated by using the WannierTools software package⁷³. The SOC effect was taken into account in all calculations.

Data availability

The data that support the findings of this study are available from the corresponding authors upon reasonable request.

Code availability

The computer codes used for the band structure calculations in this study are available from the corresponding authors upon reasonable request.

Acknowledgements

This work was supported by the Deutsche Forschungsgemeinschaft under Grant SFB 1143 (project C04) and the Würzburg-Dresden Cluster of Excellence on Complexity and Topology in Quantum Matter – *ct.qmat* (EXC 2147, project ID 390858490). R.L. was supported by the Ministry of Science and Technology of China (Grant No. 2022YFA1402704). Z.H.L. acknowledges the support by the National Key R&D Program of China (Grant No. 2022YFB3608000), the National Natu-

ral Science Foundation of China (Grant No. 12222413), and the Natural Science Foundation of Shanghai (Grants No. 23ZR1482200 and No. 22ZR1473300). B.B. acknowledges the support from the BMBF via project UKRATOP. H.C.L. was supported by the National Natural Science Foundation of China (Grants No. 11822412 and No. 11774423), the Ministry of Science and Technology of China (Grant No. 2018YFE0202600), and the Beijing Natural Science Foundation (Grant No. Z200005).

Author contributions

R.L., H.M.W., H.C.L. and S.C.W. conceived the projects. Z.J.T., Q.W. and H.C.L. synthesized the single crystals and performed electrical transport measurements. B.J., Y.J.S., R.L., W.H.S. and A.F. processed the sample surfaces. R.L., W.H.S., A.F., M.L., Z.H.L. and X.Z.C. conducted ARPES measurements. L.Q.Z. and H.M.W. performed band structure calculations. R.L., W.H.S., H.M.W., H.C.L. and S.C.W. analysed the experimental data. R.L. wrote the manuscript with input from all the authors.

Competing interests

The authors declare no competing interests.

Additional information

Supplementary information is available in the online version of the paper.

Correspondence and requests for materials should be addressed to Rui Lou, Hongming Weng, Hechang Lei or Shancai Wang.

References

1. Keimer, B., Kivelson, S., Norman, M., Uchida, S. & Zaanen, J. From quantum matter to high-temperature superconductivity in copper oxides. *Nature* **518**, 179-186 (2015).
2. Fernandes, R. M. et al. Iron pnictides and chalcogenides: a new paradigm for superconductivity. *Nature* **601**, 35-44 (2022).
3. Ye, L. et al. Massive Dirac fermions in a ferromagnetic kagome metal. *Nature* **555**, 638-642 (2018).
4. Hou, Z. et al. Observation of various and spontaneous magnetic skyrmionic bubbles at room temperature in a frustrated kagome magnet with uniaxial magnetic anisotropy. *Adv. Mater.* **29**, 1701144 (2017).
5. Kang, M. et al. Dirac fermions and flat bands in the ideal kagome metal FeSn. *Nat. Mater.* **19**, 163-169 (2020).
6. Han, M. et al. Evidence of two-dimensional flat band at the surface of antiferromagnetic kagome metal FeSn. *Nat. Commun.* **12**, 5345 (2021).
7. Nakatsuji, S., Kiyohara, N. & Higo, T. Large anomalous Hall effect in a non-collinear antiferromagnet at room temperature. *Nature* **527**, 212-215 (2015).

8. Kuroda, K. et al. Evidence for magnetic Weyl fermions in a correlated metal. *Nat. Mater.* **16**, 1090-1095 (2017).
9. Nayak, A. K. et al. Large anomalous Hall effect driven by non-vanishing Berry curvature in non-collinear antiferromagnet Mn_3Ge . *Sci. Adv.* **2**, e1501870 (2016).
10. Kiyohara, N., Tomita, T. & Nakatsuji, S. Giant anomalous Hall effect in the chiral antiferromagnet Mn_3Ge . *Phys. Rev. Appl.* **5**, 064009 (2016).
11. Yin, J.-X. et al. Quantum-limit chern topological magnetism in TbMn_6Sn_6 . *Nature* **583**, 533-536 (2020).
12. Liu, E. et al. Giant anomalous Hall effect in a ferromagnetic kagome-lattice semimetal. *Nat. Phys.* **14**, 1125-1131 (2018).
13. Wang, Q. et al. Large intrinsic anomalous Hall effect in half-metallic ferromagnet $\text{Co}_3\text{Sn}_2\text{S}_2$ with magnetic Weyl fermions. *Nat. Commun.* **9**, 3681 (2018).
14. Liu, D. F. et al. Magnetic Weyl semimetal phase in a kagome crystal. *Science* **365**, 1282-1285 (2019).
15. Ortiz, B. R. et al. New kagome prototype materials: discovery of KV_3Sb_5 , RbV_3Sb_5 , and CsV_3Sb_5 . *Phys. Rev. Mater.* **3**, 094407 (2019).
16. Ortiz, B. R. et al. CsV_3Sb_5 : a Z_2 topological kagome metal with a superconducting ground state. *Phys. Rev. Lett.* **125**, 247002 (2020).

17. Ortiz, B. R. et al. Superconductivity in the Z_2 kagome metal KV_3Sb_5 . *Phys. Rev. Mater.* **5**, 034801 (2021).
18. Yin, Q. W. et al. Superconductivity and normal-state properties of kagome metal RbV_3Sb_5 single crystals. *Chin. Phys. Lett.* **38**, 037403 (2021).
19. Xu, H.-S. et al. Multiband superconductivity with sign-preserving order parameter in kagome superconductor CsV_3Sb_5 . *Phys. Rev. Lett.* **127**, 187004 (2021).
20. Zhao, H. et al. Cascade of correlated electron states in the kagome superconductor CsV_3Sb_5 . *Nature* **599**, 216-221 (2021).
21. Chen, H. et al. Roton pair density wave in a strong-coupling kagome superconductor. *Nature* **599**, 222-228 (2021).
22. Nie, L. et al. Charge-density-wave-driven electronic nematicity in a kagome superconductor. *Nature* **604**, 59-64 (2022).
23. Xiang, Y. et al. Twofold symmetry of c -axis resistivity in topological kagome superconductor CsV_3Sb_5 with in-plane rotating magnetic field. *Nat. Commun.* **12**, 6727 (2021).
24. Li, H. et al. Rotation symmetry breaking in the normal state of a kagome superconductor KV_3Sb_5 . *Nat. Phys.* **18**, 265-270 (2022).
25. Liang, Z. et al. Three-dimensional charge density wave and surface-dependent vortex-core states in a kagome superconductor CsV_3Sb_5 . *Phys. Rev. X* **11**, 031026 (2021).

26. Jiang, Y. X. et al. Unconventional chiral charge order in kagome superconductor KV_3Sb_5 . *Nat. Mater.* **20**, 1353-1357 (2021).
27. Li, H. X. et al. Observation of unconventional charge density wave without acoustic phonon anomaly in kagome superconductors AV_3Sb_5 ($A = Rb, Cs$). *Phys. Rev. X* **11**, 031050 (2021).
28. Lou, R. et al. Charge-density-wave-induced peak-dip-hump structure and the multiband superconductivity in a kagome superconductor CsV_3Sb_5 . *Phys. Rev. Lett.* **128**, 036402 (2022).
29. Mielke, C. et al. Time-reversal symmetry-breaking charge order in a kagome superconductor. *Nature* **602**, 245-250 (2022).
30. Ortiz, B. R. et al. Fermi surface mapping and the nature of charge-density-wave order in the kagome superconductor CsV_3Sb_5 . *Phys. Rev. X* **11**, 041030 (2021).
31. Li, H. et al. Discovery of conjoined charge density waves in the kagome superconductor CsV_3Sb_5 . *Nat. Commun.* **13**, 6348 (2022).
32. Zhou, X. et al. Origin of charge density wave in the kagome metal CsV_3Sb_5 as revealed by optical spectroscopy. *Phys. Rev. B* **104**, L041101 (2021).
33. Tan, H. et al. Charge density waves and electronic properties of superconducting kagome metals. *Phys. Rev. Lett.* **127**, 046401 (2021).
34. Park, T., Ye, M. & Balents, L. Electronic instabilities of kagome metals: saddle points and Landau theory. *Phys. Rev. B* **104**, 035142 (2021).

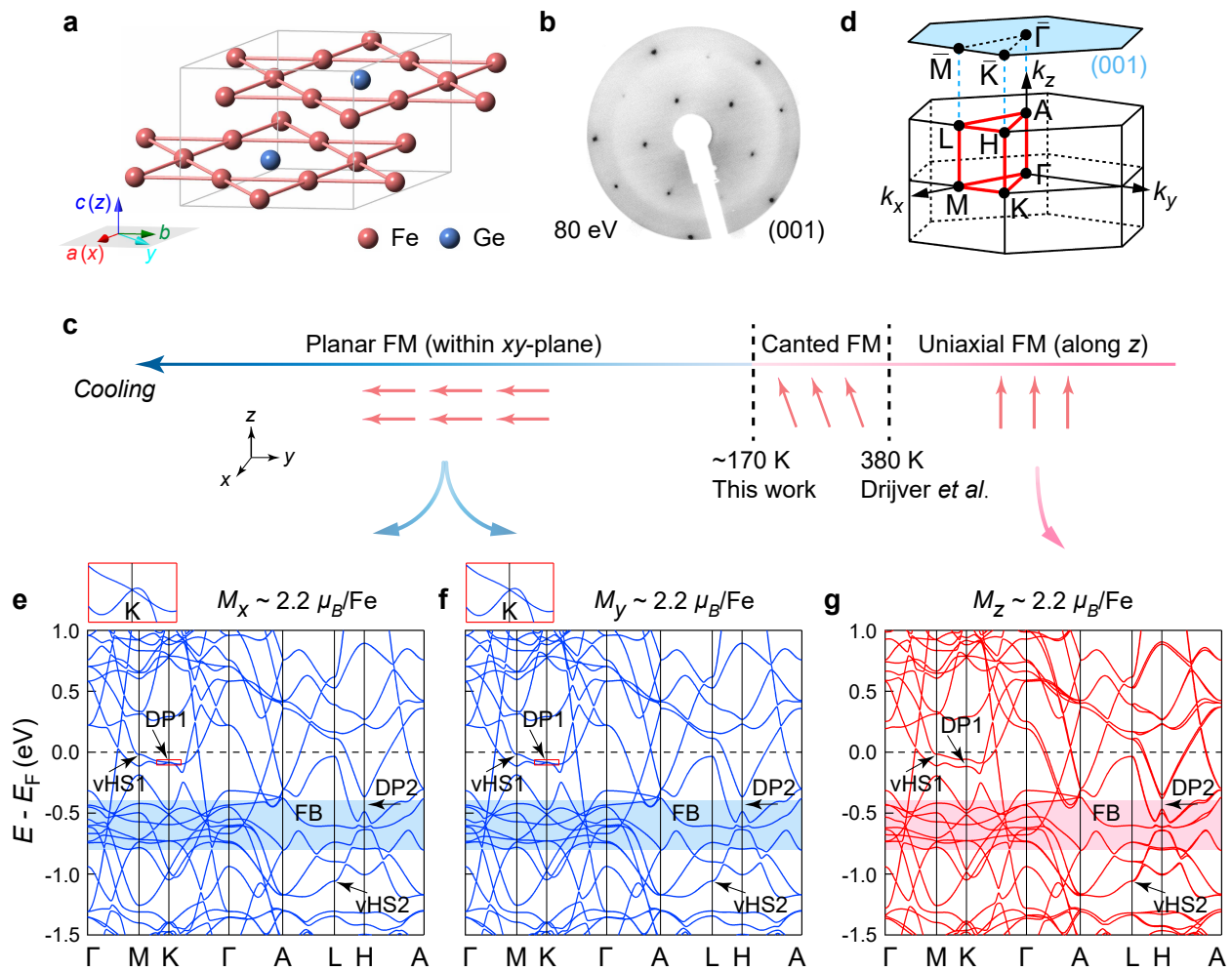
35. Christensen, M. H., Birol, T., Andersen, B. M. & Fernandes, R. M. Theory of the charge density wave in AV_3Sb_5 kagome metals. *Phys. Rev. B* **104**, 214513 (2021).
36. Denner, M. M., Thomale, R. & Neupert, T. Analysis of charge order in the kagome metal AV_3Sb_5 ($A = K, Rb, Cs$). *Phys. Rev. Lett.* **127**, 217601 (2021).
37. Lin, Y.-P. & Nandkishore, R. M. Complex charge density waves at van Hove singularity on hexagonal lattices: Haldane-model phase diagram and potential realization in the kagome metals AV_3Sb_5 ($A = K, Rb, Cs$). *Phys. Rev. B* **104**, 045122 (2021).
38. Teng, X. et al. Discovery of charge density wave in a kagome lattice antiferromagnet. *Nature* **609**, 490-495 (2022).
39. Yin, J.-X. et al. Discovery of charge order and corresponding edge state in kagome magnet FeGe. *Phys. Rev. Lett.* **129**, 166401 (2022).
40. Miao, H. et al. Spin-phonon coupling driven charge density wave in a kagome magnet. Preprint at <https://arxiv.org/abs/2210.06359> (2022).
41. Teng, X. et al. Magnetism and charge density wave order in kagome FeGe. *Nat. Phys.* **19**, 814-822 (2023).
42. Ohoyama, T., Kanematsu, K. & Yasukōchi, K. A new intermetallic compound FeGe. *J. Phys. Soc. Jpn.* **18**, 589-589 (1963).
43. Bernhard, J., Lebech, B. & Beckman, O. Neutron diffraction studies of the low-temperature magnetic structure of hexagonal FeGe. *J. Phys. F: Met. Phys.* **14**, 2379-2393 (1984).

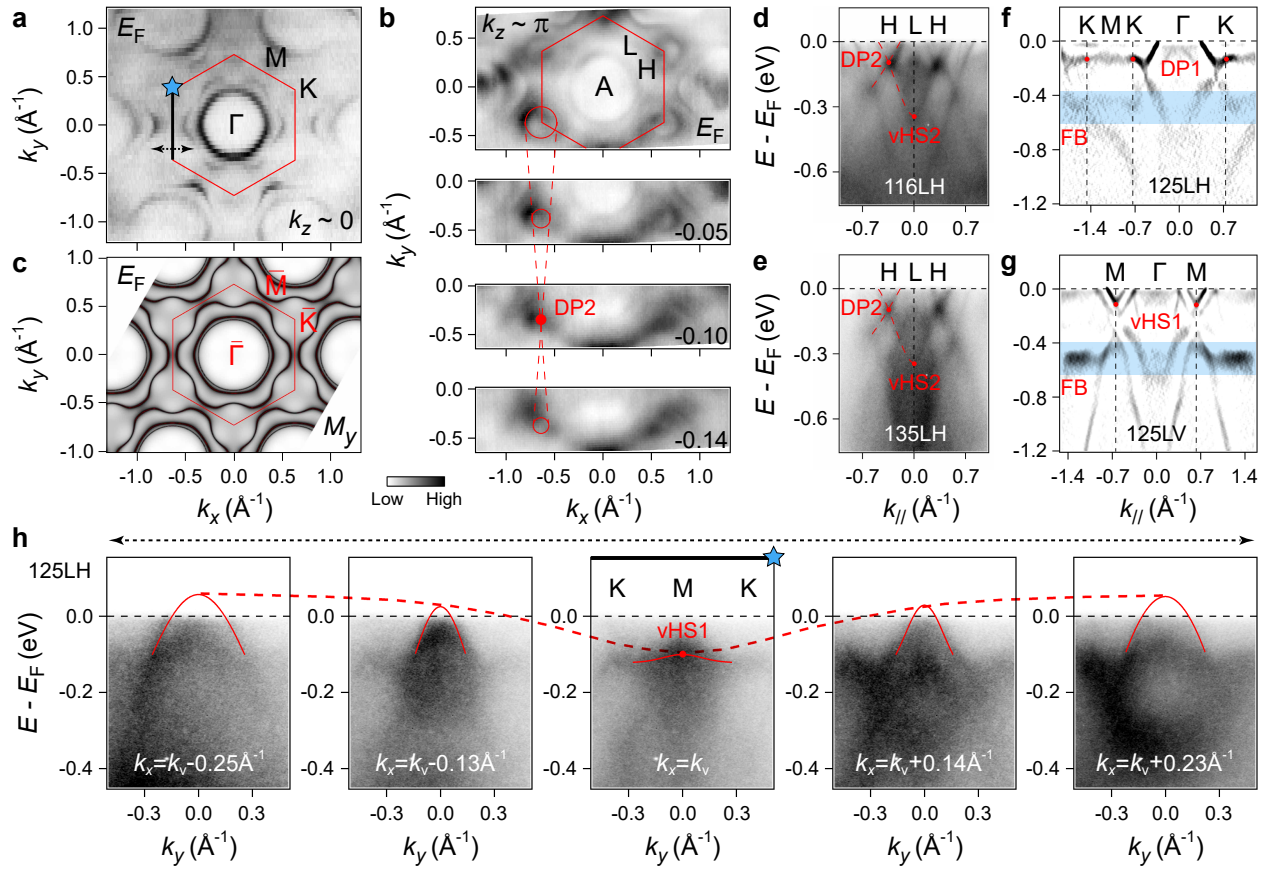
44. Drijver, J. W., Sinnema, S. G. & van der Woude, F. Magnetic properties of hexagonal and cubic Fe₃Ge. *J. Phys. F: Met. Phys.* **6**, 2165-2177 (1976).
45. Hong, D. et al. Synthesis of antiferromagnetic Weyl semimetal Mn₃Ge on insulating substrates by electron beam assisted molecular beam epitaxy. *APL Mater.* **10**, 101113 (2022).
46. Tang, C.-Y. et al. Atomically flat surface preparation for surface-sensitive technologies. *Chin. Phys. B* **29**, 028101 (2020).
47. Kanematsu, K. & Ohoyama, T. Magnetic and x-ray studies of iron-germanium system II. phase diagram and magnetism of each phase. *J. Phys. Soc. Jpn.* **20**, 236-242 (1965).
48. Guo, H. M. & Franz, M. Topological insulator on the kagome lattice. *Phys. Rev. B* **80**, 113102 (2009).
49. Kiesel, M. L. & Thomale, R. Sublattice interference in the kagome Hubbard model. *Phys. Rev. B* **86**, 121105(R) (2012).
50. Kiesel, M. L., Platt, C. & Thomale, R. Unconventional Fermi surface instabilities in the kagome Hubbard model. *Phys. Rev. Lett.* **110**, 126405 (2013).
51. Kumigashira, H. et al. High-resolution angle-resolved photoemission study of LaSb. *Phys. Rev. B* **58**, 7675 (1998).
52. Strocov, V. N. Intrinsic accuracy in 3-dimensional photoemission band mapping. *J. Electron Spectrosc. Relat. Phenom.* **130**, 65-78 (2003).

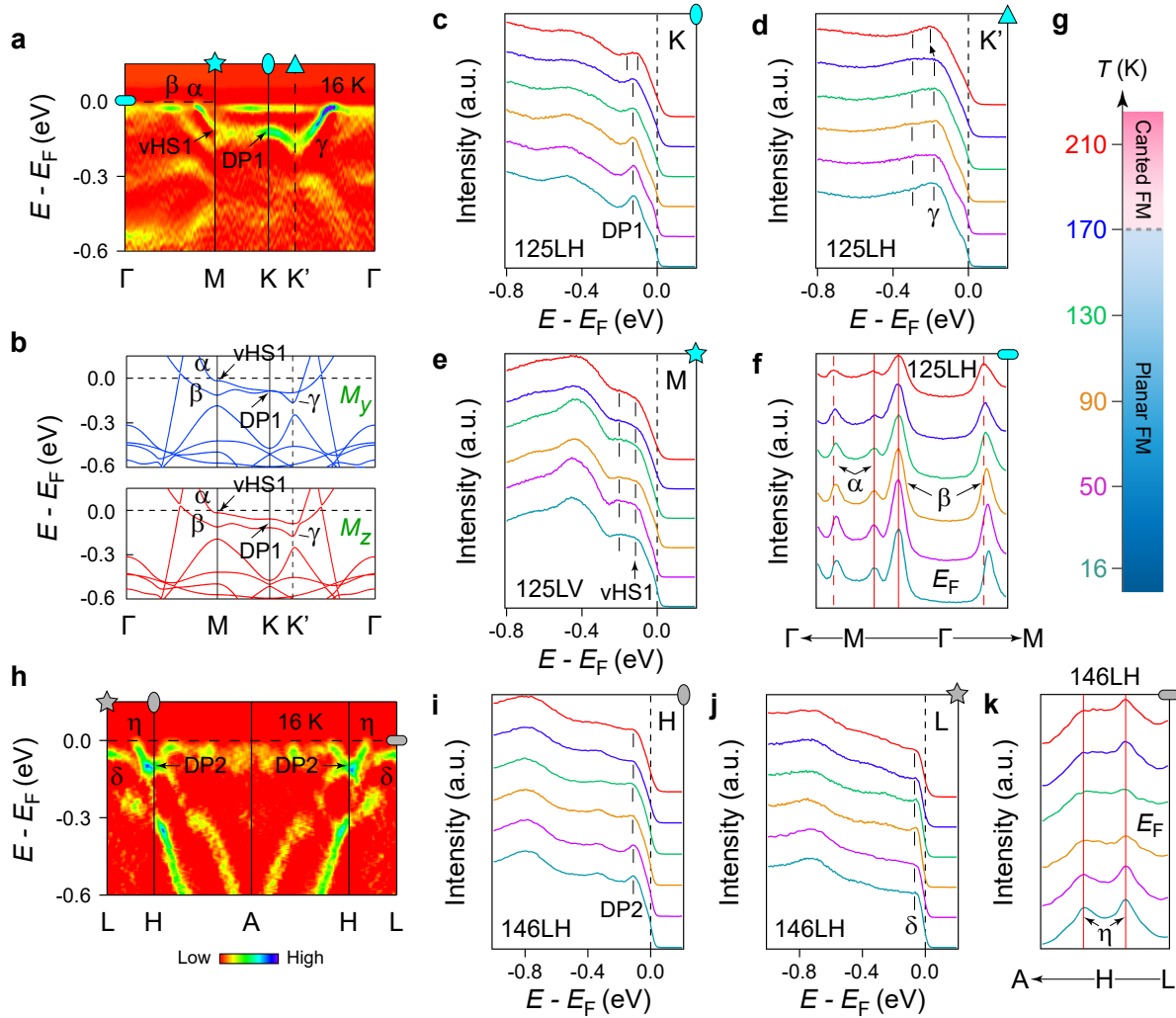
53. Wu, L., Hu, Y., Wang, D. & Wan, X. G. Novel three-dimensional Fermi surface and electron-correlation-induced charge density wave in FeGe. Preprint at <https://arxiv.org/abs/2302.03622> (2023).
54. Xie, Y. et al. Spin excitations in metallic kagome lattice FeSn and CoSn. *Commun. Phys.* **4**, 240 (2021).
55. Lin, Z. et al. Dirac fermions in antiferromagnetic FeSn kagome lattices with combined space inversion and time-reversal symmetry. *Phys. Rev. B* **102**, 155103 (2020).
56. Li, M. et al. Dirac cone, flat band and saddle point in kagome magnet YMn_6Sn_6 . *Nat. Commun.* **12**, 3129 (2021).
57. Liu, Z. et al. Electronic correlation effects in the kagome magnet GdMn_6Sn_6 . *Phys. Rev. B* **104**, 115122 (2021).
58. Gu, X. et al. Robust kagome electronic structure in the topological quantum magnets XMn_6Sn_6 ($X = \text{Dy}, \text{Tb}, \text{Gd}, \text{Y}$). *Phys. Rev. B* **105**, 155108 (2022).
59. Kane, C. L. & Mele, E. J. Quantum spin Hall effect in graphene. *Phys. Rev. Lett.* **95**, 226801 (2005).
60. Ohgushi, K., Murakami, S. & Nagaosa, N. Spin anisotropy and quantum Hall effect in the kagomé lattice: Chiral spin state based on a ferromagnet. *Phys. Rev. B* **62**, R6065(R) (2000).
61. Yin, J.-X. et al. Giant and anisotropic many-body spin-orbit tunability in a strongly correlated kagome magnet. *Nature* **562**, 91-95 (2018).

62. Neupert, T., Denner, M. M., Yin, J.-X., Thomale, R. & Hasan, M. Z. Charge order and superconductivity in kagome materials. *Nat. Phys.* **18**, 137-143 (2022).
63. Yin, J.-X., Lian, B. & Hasan, M. Z. Topological kagome magnets and superconductors. *Nature* **612**, 647-657 (2022).
64. Setty, C. et al. Electron correlations and charge density wave in the topological kagome metal FeGe. Preprint at <https://arxiv.org/abs/2203.01930> (2022).
65. Kang, M. et al. Twofold van Hove singularity and origin of charge order in topological kagome superconductor CsV₃Sb₅. *Nat. Phys.* **18**, 301-308 (2022).
66. Ma, H.-Y., Yin, J.-X., Hasan, M. Z. & Liu, J. P. Theory for charge density wave and orbital-flux state in antiferromagnetic kagome metal FeGe. Preprint at <https://arxiv.org/abs/2303.02824> (2023).
67. Wang, Y. L. Enhanced spin-polarization via partial Ge1-dimerization as the driving force of the 2×2×2 CDW in FeGe. Preprint at <https://arxiv.org/abs/2304.01604> (2023).
68. Li, H. et al. Manipulation of Dirac band curvature and momentum-dependent g factor in a kagome magnet. *Nat. Phys.* **18**, 644-649 (2022).
69. Kresse, G. & Furthmüller, J. Efficient iterative schemes for *ab initio* total-energy calculations using a plane-wave basis set. *Phys. Rev. B* **54**, 11169 (1996).
70. Kresse, G. & Joubert, D. From ultrasoft pseudopotentials to the projector augmented-wave method. *Phys. Rev. B* **59**, 1758 (1999).

71. Perdew, J. P., Burke, K. & Ernzerhof, M. Generalized gradient approximation made simple. *Phys. Rev. Lett.* **77**, 3865 (1996).
72. Mostofi, A. A. et al. An updated version of Wannier90: a tool for obtaining maximally-localised Wannier functions. *Comput. Phys. Commun.* **185**, 2309-2310 (2014).
73. Wu, Q., Zhang, S., Song, H.-F., Troyer, M. & Soluyanov, A. A. WannierTools: an open-source software package for novel topological materials. *Comput. Phys. Commun.* **224**, 405-416 (2018).







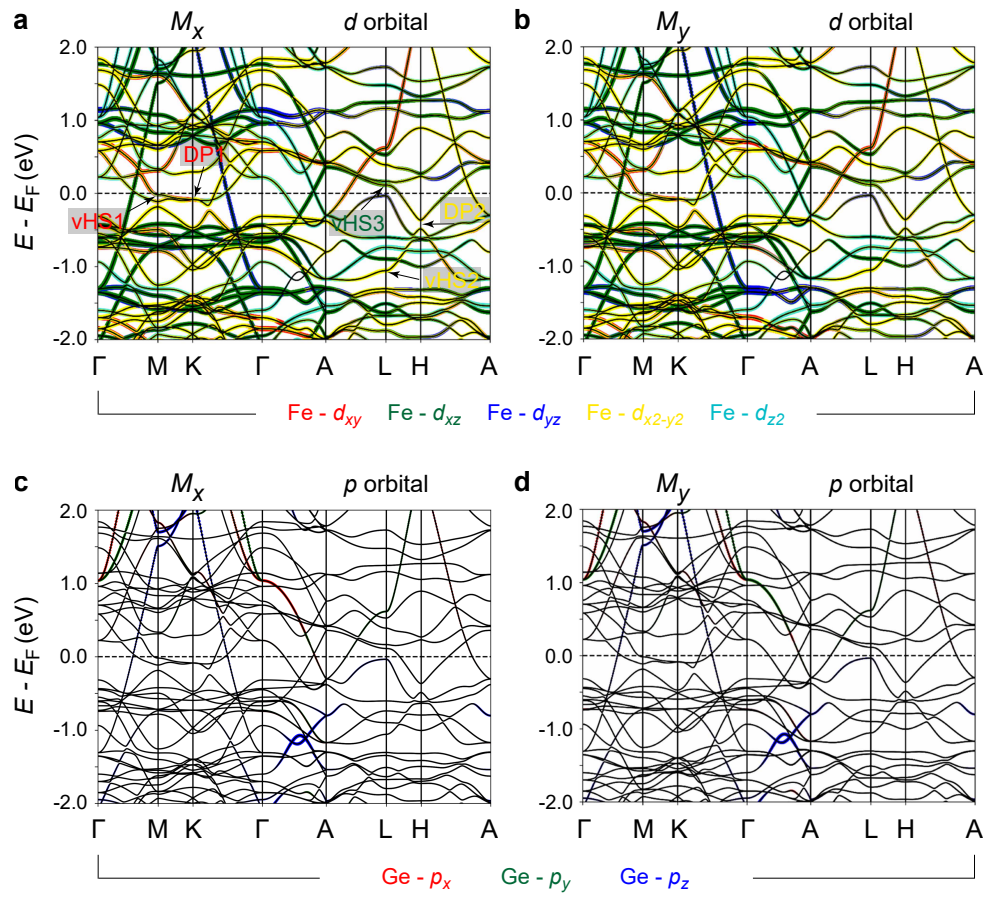


Figure 1 Crystal structure, magnetism, and band calculations. **a**, Schematic crystal structure of Fe_3Ge . The inset illustrates the setup of the x , y , and z axes relative to the a , b , and c axes, where the x and z axes are along the a and c axes, respectively, the y axis is in the ab plane, at an angle of 30° to the b axis. **b**, LEED pattern of the treated Fe_3Ge -(001) surface taken with an electron energy of 80 eV at room temperature. **c**, A summary of the magnetic phase transitions as a function of temperature in Fe_3Ge . **d**, Bulk and (001)-projected BZs with the high-symmetry points. **e–g**, DFT calculated band structures of Fe_3Ge in the FM phase for the Fe moments ($\mu_{\text{Fe}} \approx 2.2 \mu_{\text{B}}$) aligned along the x (**e**), y (**f**), and z (**g**) axis, respectively. As guided by the curved arrows, one can find the correspondence between the band calculations and the temperature axis in **c**. Two sets of DPs and vHSs below E_{F} are highlighted by the black arrows. The FB regions at around -0.5 eV are marked out by the blue and red shades. As indicated by the red rectangles in **e** and **f**, the insets of which show the enlarged view of the nearly gapless (~ 0.5 meV) DP1 at K point in the planar FM state.

Figure 2 Typical band structure of the kagome lattice. **a**, FS mapping of Fe_3Ge taken by the 125-eV photons (close to $k_z = 0$ plane) with linear horizontal (LH) polarization. **b**, Constant-energy ARPES intensity plots ($h\nu = 146$ eV, close to $k_z = \pi$ plane, LH polarization) at the energies of 0, -0.05 , -0.10 , and -0.14 eV, respectively. The red circles indicate the Dirac pocket at H point. As guided by the red dashed lines, the Dirac pocket shrinks and reopens as the energy crosses the DP2. **c**, Projections of DFT calculated bulk FSs on the (001) surface of Fe_3Ge . The calculations were carried out by considering

a FM moment ($\mu_{\text{Fe}} \approx 2.2 \mu_{\text{B}}$) aligned along the y axis. **d,e**, ARPES intensity plots measured along the H - L - H directions with the photon energies of 116 (**d**) and 135 eV (**e**), respectively (LH polarization). The red dashed curves are guides to the eye for the Dirac cone structure of the DP2 at H point and its connecting to the vHS2 at L point. Although the k_z value of the 135-eV photons is not that close to $k_z = \pi$ plane (Supplementary Fig. S4a), the ARPES spectra are analogous to that under the 116-eV photons due to the k_z broadening effect. For convenience, we use the BZ notation of $k_z = \pi$ plane for the 135-eV data. **f,g**, Second derivative intensity plots taken along the Γ - K - M (**f**) and Γ - M (**g**) directions, respectively. The 125-eV photons with LH (**f**) and linear vertical (LV) (**g**) polarizations were utilized. The less-dispersive DP1 at K point, the vHS1 at M point, and the FB regions are marked out. **h**, Dispersions across the vHS1. As guided by the black dashed arrows in **a** and **h**, these cuts are recorded along the k_y directions at $k_x = k_v - 0.25 \text{ \AA}^{-1}$, $k_v - 0.13 \text{ \AA}^{-1}$, k_v , $k_v + 0.14 \text{ \AA}^{-1}$, and $k_v + 0.23 \text{ \AA}^{-1}$, respectively. The blue star marker and thick black line indicate the cut along the K - M - K direction. The red solid and dashed curves mark out the dispersions of the vHS1 along the k_y and k_x directions, respectively.

Figure 3 Spectroscopic signature of the spin-reorientation effect. **a**, A summary of the band structures (second derivative intensity plots) of Fe_3Ge along the Γ - M - K - Γ lines ($h\nu = 125 \text{ eV}$, $T = 16 \text{ K}$). The cyan markers indicate the locations where the EDCs (ellipse, triangle, and star markers) and MDCs (capsule-like marker) in **c-f** are extracted. **b**, Comparison between the calculated bands near E_{F} (Γ - M - K - Γ lines) of FM Fe_3Ge with

the Fe moments ($\mu_{\text{Fe}} \approx 2.2 \mu_{\text{B}}$) along the y (upper panel) and z (lower panel) axes. **c–e**, Temperature-dependent EDCs taken at K (**c**), K' (**d**), and M (**e**) points, respectively. The black dashes are extracted peak positions. The black arrow in **d** illustrates the downward shift of the γ band. In **e**, the LV-polarized light was used to better reveal the β band bottom at M point. **f**, Temperature-dependent MDCs along the Γ - M direction taken at E_{F} . To better visualize the evolutions of the MDC peaks, we align one of the α, β bands branches at various temperatures to a certain momentum position, respectively, as indicated by the red solid lines. **g**, Magnetic phase diagram of Fe_3Ge based on our temperature-dependent measurements. **h**, Second derivative intensity plot measured along the A - H - L lines ($h\nu = 146$ eV, $T = 16$ K). The grey markers indicate the locations where the EDCs (ellipse and star markers) and MDCs (capsule-like marker) in **i–k** are extracted. **i, j**, Temperature-dependent EDCs taken at H (**i**) and L (**j**) points, respectively. The black dashes are extracted peak positions. **k**, Temperature-dependent MDCs along the A - H - L direction taken at E_{F} . The red solid lines indicate the less temperature-sensitive k_{F} 's of the η band.

Figure 4 Orbital-resolved band structure. **a, b**, DFT band structure calculations of FM Fe_3Ge for the Fe moments ($\mu_{\text{Fe}} \approx 2.2 \mu_{\text{B}}$) aligned along the x (**a**) and y (**b**) axes with the Fe-3d orbital projections, respectively. The red, green, blue, yellow, and turquoise colours represent the d_{xy} , d_{xz} , d_{yz} , $d_{x^2-y^2}$, and d_{z^2} orbitals, respectively. The DP1,2 and vHS1,2 below E_{F} as well as the vHS3 slightly above E_{F} are marked out in **a**. **c, d**, Same as **a, b**

with the Ge-4*p* orbital projections. The red, green, and blue colours represent the p_x , p_y , and p_z orbitals, respectively.